

## Article

# Thermal Stability and Utilization of 1D-Nanostructured $\text{Co}_3\text{O}_4$ Rods Derived by Simple Solvothermal Processing

Vilko Mandić <sup>1,\*</sup> , Stanislav Kurajica <sup>1</sup> , Milivoj Plodinec <sup>2</sup> and Ivana Panžić <sup>1</sup> 

<sup>1</sup> Department of Inorganic Chemical Technology and Nonmetals, Faculty of Chemical Engineering and Technology, University of Zagreb, Marulićev trg 20, 10000 Zagreb, Croatia

<sup>2</sup> Department of Chemistry and Applied Bioscience, ScopeM, Eidgenössische Technische Hochschule Zürich, Auguste-Piccard-Hof 1, 8093 Zürich, Switzerland

\* Correspondence: vmandic@fkit.hr; Tel.: +385-1-4597-226

**Abstract:** For p-type semiconductor nanoparticles, such as the cobalt oxide spinel, enhancing the nanoparticle geometry can expose more of the surface and bring up the sensitivity and applicability, pointing to even more advantageous behaviour in comparison to n-type semiconductors which are known for a somewhat faster reactivity. Here, we present a strategy that relies on fostering a simple synthetic route that can deliver reasonably or comparably performing p-type-semiconducting partially 1D- $\text{Co}_3\text{O}_4$  material prepared under less technically and economically demanding conditions. Structurally monophasic  $\text{Co}_3\text{O}_4$  nanoparticles with a spinel structure were indicated by powder X-ray diffraction, while the presence of traces of organic-phase residuals in otherwise chemically homogeneous material was observed by Fourier-transform infrared spectroscopy. Scanning electron microscopy further showed that the observed fine nanoparticle matter formed agglomerates with the possible presence of rod-like formations. Interestingly, using transmission electron microscopy, it was possible to reveal that the agglomerates of the fine nanoparticulated material were actually nanostructured, i.e., the presence of 1D-shaped  $\text{Co}_3\text{O}_4$  rods embedded in fine nanoparticulated matrix was confirmed. In conjunction with the  $\text{N}_2$  adsorption–desorption isotherms, discussion about the orientation, exposure of nanostructured rod domains, and derivative geometry parameters was possible. The nanostructured  $\text{Co}_3\text{O}_4$  material was shown to be stable up to 800 °C whereat the decomposition to CoO takes place. The specific surface area of the nanostructured sample was raised. For the purpose of testing the photoactivity of the prepared samples, simple sorption/photodegradation tests using methylene blue as the model pollutant were performed. The degradation performance of the prepared nanostructured  $\text{Co}_3\text{O}_4$  was better described by a pseudo-second-order fit, suggesting that the prepared material is worth further development toward improved and stable immobilized photocatalysts.

**Keywords:** cobalt spine; p-semiconductor; photocatalysts; nanostructured; transmission electron microscopy



**Citation:** Mandić, V.; Kurajica, S.; Plodinec, M.; Panžić, I. Thermal Stability and Utilization of 1D-Nanostructured  $\text{Co}_3\text{O}_4$  Rods Derived by Simple Solvothermal Processing. *Catalysts* **2022**, *12*, 1162. <https://doi.org/10.3390/catal12101162>

Academic Editors: Amr Fouda and Mohammed F. Hamza

Received: 9 September 2022

Accepted: 30 September 2022

Published: 2 October 2022

**Publisher's Note:** MDPI stays neutral with regard to jurisdictional claims in published maps and institutional affiliations.



**Copyright:** © 2022 by the authors. Licensee MDPI, Basel, Switzerland. This article is an open access article distributed under the terms and conditions of the Creative Commons Attribution (CC BY) license (<https://creativecommons.org/licenses/by/4.0/>).

## 1. Introduction

Semiconducting materials based on mixed metal oxides are convenient for application as gas sensors, photocatalysts, or photovoltaics, due to some of their unique properties but also some quite general advantages. Namely, gas sensors require materials with a vapour-sensitive surface, photocatalytic systems require materials with an oxygen-sensitive surface, and photovoltaic devices require materials with a photon-sensitive surface. The unique properties are specific electronic structure properties yielding specific bandgaps and specific surface reactivity conditions, while general advantages are the ability to be derived over a low-price synthesis, into a robust material, whose thermodynamics and reaction mechanisms are well known and are widely applicable.

Among various metal-oxide-based materials for interaction with harmful or toxic gases, various n-type semiconductor materials ( $\text{SnO}_2$ , ZnO,  $\text{TiO}_2$ ,  $\text{WO}_3$ ,  $\text{In}_2\text{O}_3$ , and  $\text{Fe}_2\text{O}_3$ ) [1–3] and

p-type semiconductor materials (NiO, CuO, Mn<sub>3</sub>O<sub>4</sub>, and Co<sub>3</sub>O<sub>4</sub>) [4–7] have emerged. Having the equivalent morphologies, n-type semiconductors are known for a somewhat faster reactivity (response), leading to a considerably lower amount of p-type semiconductor-related reports [7]. Among those, a cobalt oxide (Co<sub>3</sub>O<sub>4</sub>) spinel is found. It is a mixed-valence spinel of CoO and Co<sub>2</sub>O<sub>3</sub> with a high-oxygen-content, p-type semiconductor with an indirect band gap in the range between 1.6 and 2.2 eV. Its p-type conductivity originates from oxygen over-stoichiometry caused by metal vacancies as well as excess interstitial oxygen. As previously suggested, Co<sub>3</sub>O<sub>4</sub> is studied for application in energy storage [8], catalysis [9], sensors [10], electrochemistry [11], magnetism [12], and gas sensing. For example, catalytic and sensing fields of application for Co<sub>3</sub>O<sub>4</sub> heavily rely on surface performance which, in turn, heavily relates to morphologic properties and thermal stability properties. Specifically, for photocatalytic performance, operation occurs under ambient conditions; for sensing performance, the operation is usually at elevated temperatures above 200 °C; for catalytic performance, operations at even higher temperatures are required [8–10]. We bring about the necessity to enhance the investigation of morphology development and thermal stability in order to show the importance of Co<sub>3</sub>O<sub>4</sub> p-type material for the abovementioned application. Namely, when electrons become trapped, charge carrier pairs are created. Under ambient conditions, oxygen species readily adsorb at the Co<sub>3</sub>O<sub>4</sub> surface, causing the creation of additional charge carriers at the surface. Oxidizing gases other than the atmospheric oxygen, O<sub>2</sub>, for example, ozone or nitrous oxide, generally tend to enhance this effect, while reducing gases tend to decrease this effect, both of which affect surface conductivity, i.e., yield a qualitative and quantitative electric signal [7,13]. Finally, the materials can be utilised in constituents of the photovoltaic devices.

There are a lot of routes reported on how to prepare Co<sub>3</sub>O<sub>4</sub> nanoparticles [14]. In general, the majority of them rely on complex, toxic, or expensive precursors, time-demanding or high-temperature processing, etc. [14]. Therefore, the solvothermal route has been recognised and is a significant milestone for simple, affordable, and convenient preparation of Co<sub>3</sub>O<sub>4</sub> nanoparticles with high purity and homogeneity [14]. To reach the area of advanced materials, conventional Co<sub>3</sub>O<sub>4</sub> nanoparticles have to be nanostructured to increase the material's specific surface area and pore volume [15,16]. In the following sections, we discuss Co<sub>3</sub>O<sub>4</sub> nanostructures according to their performance for superstructured morphologies from zero-dimensional (0D) nanoparticles to three-dimensional (3D) networks, but with a focus on 1D nanoformations. Among nanostructured Co<sub>3</sub>O<sub>4</sub> materials, the architectures of 1D Co<sub>3</sub>O<sub>4</sub> nanorods, hollow nanotubes, porous nanowires, and nanofibers were evidenced as promising for advanced materials application. Of all the three mentioned areas where the Co<sub>3</sub>O<sub>4</sub> nanostructures can be utilised, the material performance greatly depends on the material's morphology and assembly. Thus, reports on the morphological control, including crystal size, external shape, surface structure, crystal orientation, controllable pore, stacking manners, aspect ratios, and even crystalline densities, are highly interesting [17,18].

Porous structures were found to be beneficial for gas sensing on behalf of increasing the surface reactive sites and facilitating the diffusion of target gases. One-dimensional nanofibers containing widely necked particles were more advantageous for achieving a high gas-sensing response with the less-elongated nanofibers showing more narrow interparticle contacts [19]; in addition, hydrothermally derived mesoporous, macroporous, and 1D Co<sub>3</sub>O<sub>4</sub> materials can have several times more effective gas-sensing than their isotropic 0D nanoparticle counterparts [20]. Choi et al. controlled the solvothermal reaction to yield cobalt-containing precursors in the form of nanorods, nanosheets, and nanocubes and converted all of them into nanostructured Co<sub>3</sub>O<sub>4</sub> without morphological variation; they observed better gas-sensing responses, which was attributed to the less agglomerated nanostructures [21].

Co<sub>3</sub>O<sub>4</sub> has been considered as a convenient candidate for the photodegradation of organic dyes in wastewater treatment due to its thermodynamic stability and other favourable properties such as low cost, easy preparation, and environmental friendliness [22]. As conventional wastewater treatment cannot completely degrade the pollutants down to non-

hazardous substances, advanced oxidation processes (AOPs) were introduced as convenient tools for eliminating various organic pollutants from water under UV–VIS irradiation in the presence of photocatalysts [23]. In contrast to the widely used TiO<sub>2</sub>-based materials, Co<sub>3</sub>O<sub>4</sub> has a narrower band gap (in the VIS part of the solar spectra, around 2 eV), better surface availability, and beneficial physical and chemical properties. The water contaminated with organic dyes discharged by various industries such as paint, textiles, paper, and plastics poses a great threat to the environment [24]. Co<sub>3</sub>O<sub>4</sub> nanoparticles exhibit enhanced catalytic activity compared to bulk Co<sub>3</sub>O<sub>4</sub>, because of their large surface-to-volume ratio, size- and shape-dependent properties, and high concentration of under-coordinated active surface sites [22,25]. In comparison to other metal oxides, the performance of Co<sub>3</sub>O<sub>4</sub> nanoparticles has been shown as advantageous many times [26–28]. Therefore, it is of great importance to control the preparation of nanosized Co<sub>3</sub>O<sub>4</sub>. Nanostructured Co<sub>3</sub>O<sub>4</sub> has even been used in all-oxide heterojunction photovoltaics [29,30].

All the above results suggest that porous 1D nanostructured Co<sub>3</sub>O<sub>4</sub> can easily serve as a highly performing material because of its high specific surface area. To prepare specifically 1D Co<sub>3</sub>O<sub>4</sub> nanoparticles, one can use the template approach, which is, again, complex or slow, whereas direct chemical deposition, electrospinning, hydrothermal, and solvothermal synthesis are more favourable. Nanostructured Co<sub>3</sub>O<sub>4</sub> can be prepared via intermediate cobalt carbonate, cobalt hydroxide, and cobalt carbonate-hydroxide, where, during their thermal annealing, the morphology becomes preserved [31–33]. It was shown that on behalf of co-precipitation followed by calcination, small nanorods 6–8 nm in diameter and 20–30 nm in length can be prepared [34]. It was found that the temperature of the solvothermal processing was the most important parameter for achieving the rhombic shape of the nanostructured 1D particles [35].

Here, we report on the simple course of solvothermal synthesis of Co<sub>3</sub>O<sub>4</sub> that allowed the preparation of nanostructured formations in the matrix. The characterisation methods focused on describing compositional and structural aspects of the derived material. The foremost important was the description of the morphologic parameters with respect to thermal stability, both of which are fundamental for photocatalytic or photovoltaic or sensing applications. Photocatalytic efficiency was confirmed under some restrictions, but more importantly, high sorption efficiency was confirmed, which can be further optimized.

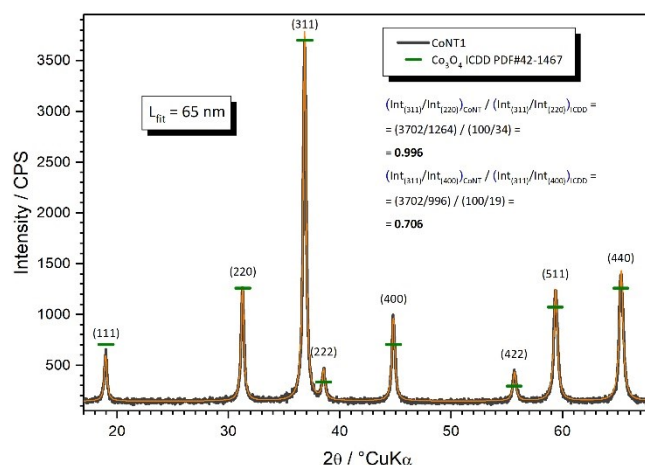
## 2. Results and Discussion

### 2.1. Phase Development and Thermal Evolution

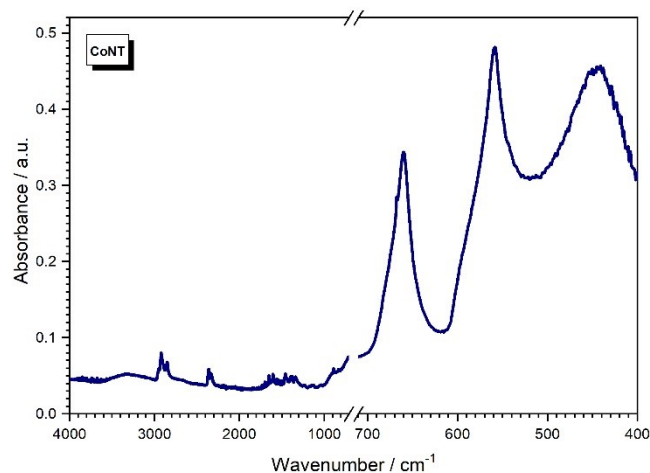
Figure 1 presents the PXRD pattern of the sample synthesized by the solvothermal method. Observed diffraction peaks at 19.00, 31.27, 36.85, 38.54, 44.81, 55.66, 59.36, 65.24, and 68.63°2 $\theta$  correspond to (111), (220), (311), (222), (400), (422), (511), (440), and (531) planes of cubic Co<sub>3</sub>O<sub>4</sub> (ICDD PDF#42-1467). There are no residual peaks corresponding to other cobalt oxide phases or unassigned peaks. As can be seen, the diffraction peaks are broad due to the nanosized crystallites. The average spinel crystallite size was calculated by the Scherrer method and yielded 65 nm. The diffractogram was fitted and, using ICDD data, the aspect ratio of the peaks was compared. The comparison coefficient of 0.996 for the (220) plane suggests complete concordance with the isotropic particle configuration of the ICDD reference. However, the comparison coefficient of 0.706 for the (400) plane suggests the opposite. It seems that the particles in the samples are statistically not isotropic. At this point, the attempts to describe the exact aspect ratio to 1D or 2D configuration would be too speculative.

Figure 2 shows the FTIR spectra of the synthesized nanoparticles in the wavenumber range of 700–500 cm<sup>−1</sup>. Two strong bands at 660 and 560 cm<sup>−1</sup> were observed. Bands at 660 and 560 cm<sup>−1</sup> are due  $\nu(\text{Co-O})$  modes and are typical for crystalline Co<sub>3</sub>O<sub>4</sub> [36]. Namely, Co<sub>3</sub>O<sub>4</sub> is a mixed-valence compound having a spinel structure with oxygen atoms arranged in a cubic close-packed structure where Co<sup>2+</sup> occupies tetragonal while Co<sup>3+</sup> takes the octahedral interstices [17]. Therefore, the peak at 660 cm<sup>−1</sup> is attributed to the

tetrahedrally coordinated  $\text{Co}^{2+}$ , while the peak at  $560\text{ cm}^{-1}$  can be assigned to octahedrally coordinated  $\text{Co}^{3+}$  [37].



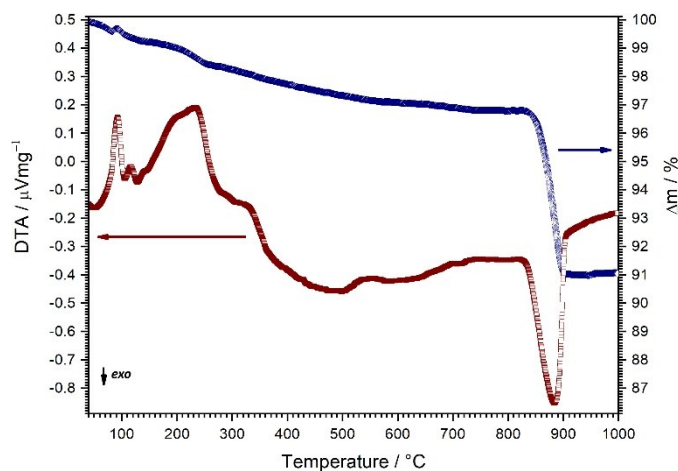
**Figure 1.** Powder X-ray diffraction pattern of the prepared  $\text{Co}_3\text{O}_4$  spinel.



**Figure 2.** Infrared ATR spectrum of the prepared  $\text{Co}_3\text{O}_4$  nanoparticles.

Thermal evolution and thermal behaviour of the derived nanoparticles were investigated by simultaneous thermal analysis that inherently provides us with more relevant information. Namely, the whole course of the sample evolution was monitored rather than properties at a given discrete state as with other methods, which makes the pinpointing of applicability ranges much more possible in order for adjustments in future experiments. Figure 3 shows TG and DTA curves in the temperature range between  $25\text{ }^\circ\text{C}$  and  $1000\text{ }^\circ\text{C}$ , recorded with a constant heating rate of  $10\text{ }^\circ\text{C min}^{-1}$ . The removal of the persisting solvents and adsorbed water is responsible for the first two endothermic peaks on the DTA curve, which are accompanied with minor mass loss observable on the TG curve. Following this, a somewhat stronger endotherm and mass loss are observed and ascribed to the decomposition of the remaining impurities related with precursors residuals. With the further increase in the heating, in the temperature range between  $820\text{ }^\circ\text{C}$  and  $910\text{ }^\circ\text{C}$ , one can observe a strong exotherm followed by considerable mass loss. These features are a consequence of the cobalt oxide spinel decomposition to cobalt (II) oxide [38]. Octahedral  $\text{Co}^{3+}$  cations undergo reduction due to the surface oxygen release at elevated temperatures in lean oxygen environments [39]. The reaction entropy is dominated by the oxygen gas release and the Gibbs energy of reaction products is decreased [40]. The sample mass loss

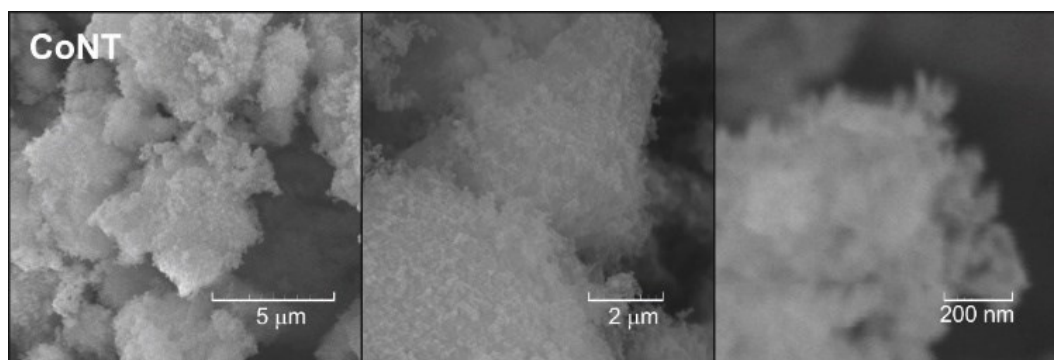
in this temperature range is 6%, which indeed roughly fits the oxygen loss in the spinel decomposition process following the equation:



**Figure 3.** TG and DTA curves of the prepared  $\text{Co}_3\text{O}_4$  nanoparticles.

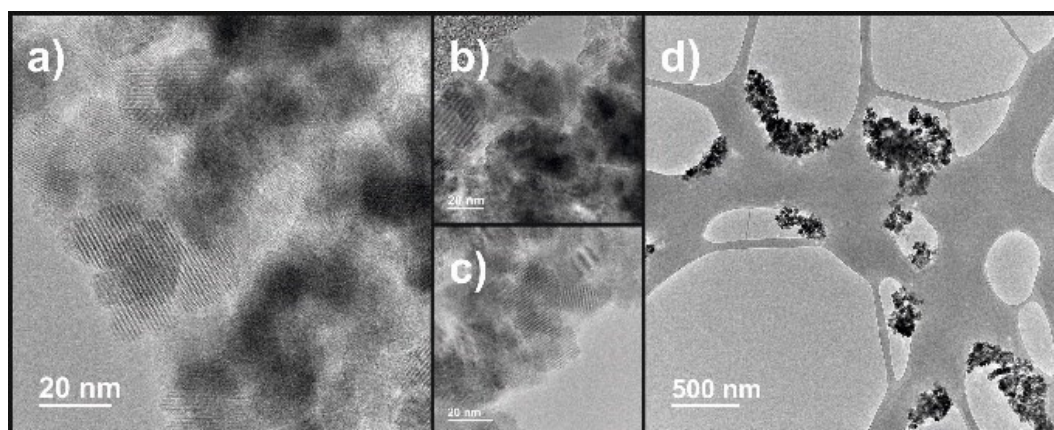
## 2.2. Morphological Characteristics

Figure 4 shows representative SEM micrographs taken at different magnifications. As can be seen, the sample consists of agglomerated particles. Higher magnifications enable closer inspection that reveals that the agglomerates actually consist of much finer particles with nonuniform nonisotropic particle shape. The agglomerates are similar in size; the magnification of the SEM micrographs is not sufficient to discuss the particle size distribution of the domains within the agglomerates beyond any doubt. However, it may be said that the particles forming agglomerates seem to have a narrow particle size distribution in the submicron range. Interestingly, one can observe that the mentioned domains may be elongated in shape. For more detail, TEM is necessary.



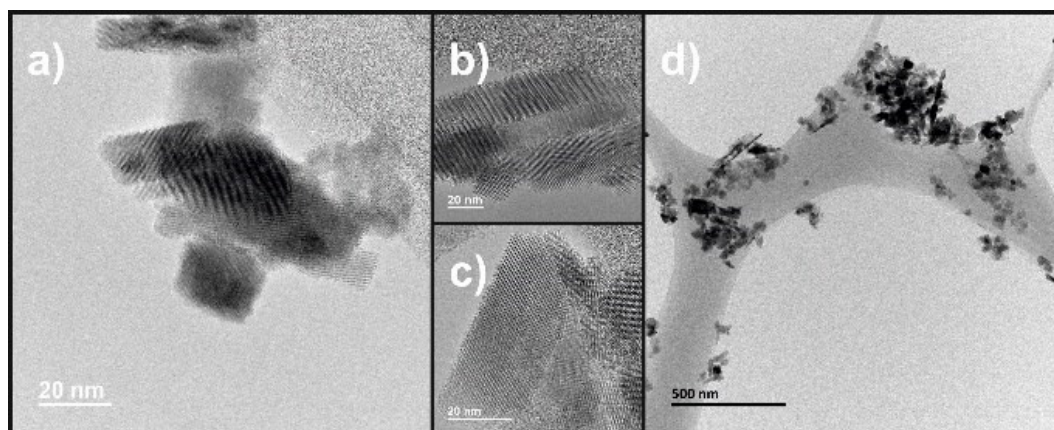
**Figure 4.** Scanning electron microscopy micrographs of the prepared  $\text{Co}_3\text{O}_4$  nanoparticles.

The transmission electron microscopy is much more revealing towards shape and size distribution of the particles that form the agglomerates. Only for the purpose of comparison of nanostructured cobalt oxide with conventional cobalt oxide nanoparticles in TEM, we prepared conventional cobalt oxide nanoparticles at a much lower temperature than of the solvothermal reaction. Figure 5a–d show those nanoparticles; the agglomerates are dispersed relatively successfully, so the domain particles are predominately isotropic with a quite narrow particle size distribution with size values centred at 25 nm. Nanoformations with specific aspect ratios (1D, 2D) are not evidenced.



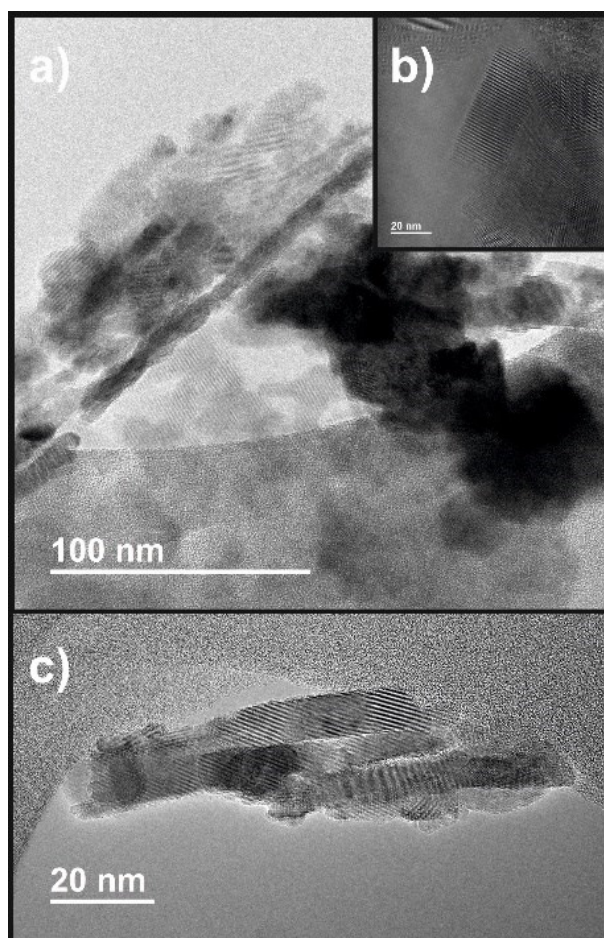
**Figure 5.** Transmission electron microscopy micrographs of the conventional  $\text{Co}_3\text{O}_4$  nanoparticles: (a)  $\text{Co}_3\text{O}_4$  nanoparticle matrix; (b)  $\text{Co}_3\text{O}_4$  nanoparticle agglomerate; (c)  $\text{Co}_3\text{O}_4$  nanoparticles fringes, and (d)  $\text{Co}_3\text{O}_4$  nanoparticle agglomerates at lower magnification.

Figure 6a–d show TEM micrographs for the nanostructured cobalt oxide spinel. In this case, the micrographs show a completely different appearance of the particles, solvothermally derived at the temperature of  $235\text{ }^\circ\text{C}$ . The average particle size distributions seem to be somewhat greater than in the case of conventional nanoparticles. In this case, one may say that some matrix is retained with more or less the same nanoparticle shape and size distribution; however, a plethora of nanoformations with a specific aspect ratio, i.e., nanorods, that are embedded in the matrix are observed. The nanorods actually range from elongated particles, nanoplates, or nanorods about  $30\text{ nm}$  in diameter and 2–3 times the length, to nanowires about  $10\text{ nm}$  in diameter and up to 10 times the length.



**Figure 6.** Transmission electron microscopy micrographs of the nanostructured  $\text{Co}_3\text{O}_4$  formations: (a) 1D  $\text{Co}_3\text{O}_4$  nanoformations; (b) ordered 1D  $\text{Co}_3\text{O}_4$  nanorods; (c) fringes for 1D  $\text{Co}_3\text{O}_4$  nanoformations, and (d) 1D  $\text{Co}_3\text{O}_4$  nanoformations agglomerates at lower magnification.

This nanostructured 1D morphology is particularly obvious from the micrographs in Figure 7a–c. Microscopy results point to lower sizes of the particles than the PXRD for the crystallites. Considering microscopy does not give average nor statistical values and considering that Scherrer is not sensitive to the crystallite aspect ratio, we think that the discrepancy between PXRD crystallite and TEM particle size determination does not exist. In addition, TEM diffraction was omitted as PXRD did not even suggest the presence of phases other than the cobalt oxide spinel. Overall, from the micrographs of the cobalt oxide spinel, one must expect considerable specific surface and thereof surface reactivity.



**Figure 7.** Transmission electron microscopy high-magnification micrographs of the prepared 1D nanostructured  $\text{Co}_3\text{O}_4$  formations: (a) 1D  $\text{Co}_3\text{O}_4$  nanoformations in nanoparticulated matrix; (b) visible fringes for 1D  $\text{Co}_3\text{O}_4$  at higher magnification; (c) 1D  $\text{Co}_3\text{O}_4$  nanoformations at higher magnification.

The nitrogen adsorption–desorption isotherm of the prepared nanostructured powder is shown in Figure 8. The isotherms follow type V adsorption–desorption, which complies with the mesoporous microstructure. Adsorption in mesoporous materials normally occurs in multilayers and is followed by capillary condensation that takes place in the mesopores. Such a condensation process is accompanied with characteristic hysteresis of the isotherms. In this particular case, the appearance of the hysteresis loop resembles the H1 type. Agglomerates or spherical particles arranged in a uniform way often make relatively connected pores with cylindrical geometry with relatively high pore size and high pore uniformity, all of which is typical for the H1 hysteresis loop [41]. Using the BET method, the specific surface area of  $44.7 \text{ m}^2 \text{ g}^{-1}$  was calculated. Using the BJH method from the desorption branch of nitrogen isotherms, the pore size distribution of the nanostructured powder was calculated. The material shows a wide bimodal pore size distribution with an average pore diameter of 20 nm, which is consistent with the nanostructured cobalt oxide spinel nanoformations embedded within the isotropic and agglomerated cobalt oxide spinel nanoparticles.

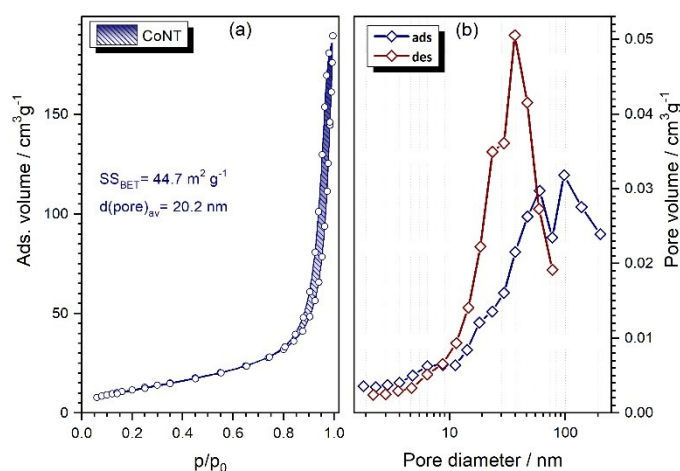


**Figure 8.** (a)  $N_2$  adsorption–desorption isotherms of  $Co_3O_4$  nanoformations; (b) pore size distribution calculated from desorption branch.

### 2.3. Intermediate Functional Properties

We performed only a simple study to prove the activity of the surface by testing the photoactivity. For the test, the photodegradation efficiency experiment was performed using the simplest setup and basic dye. The change in the dye concentration vs. reaction time (30 min in dark and 60 min of irradiation) was measured. Figure 9 presents the MB dye degradation ratio. Considerable degradation activity was noted in the first 30 min of the process and was attributed to sorption in the dark. After an additional 60 min of irradiation, the nanostructured cobalt oxide photocatalyst reached almost complete photodegradation. Both the adsorption and the photodegradation part of the experiment were governed by the small amount of the sample available, so the experimental setup with respect to the available reaction chamber was scaled down to the best of our capabilities. Therefore, we were able to collect a relatively small amount of concentration measurement of the dye for the experiment graph (Figure 9). The data were fitted to pseudo-first- and pseudo-second-order kinetic processes. The constant ( $k$ ) was obtained from the slope of the linear fit  $-\ln(C/C_0)$  vs. reaction time, and for the pseudo-second from the linear fit  $(1/C - 1/C_0)$  vs. reaction time. The kinetic constant of  $k = 0.00155 \pm 0.00021 L \cdot mg^{-1} \cdot min^{-1}$  and the  $R^2 = 94.569\%$  were better for the pseudo-second-order, indicating that our photocatalytic process was governed by more factors than just the pollutant concentration, such as light intensity and by-products formation [42]. We consider that it serves as a point for indicating the sorption and photocatalytic activity, but does not allow discussion of the reaction mechanisms. Namely, it is necessary to point out that the experiment surely suffers from some loss (filter-related losses for each measurement of the concentration) of the powdered material, so the results must be taken relatively, i.e., absolute values for adsorption in the dark may be marginally underestimated but the absolute values for subsequent photodegradation are surely underestimated. Hence, the values for sorption activity are probably quite believable but the values for the extent of the photocatalytic activity of the nanostructured cobalt oxide spinel can only serve as an indicator. Because of the abovementioned boundaries, conducting and comparing the sorption/degradation experiment for the isotropic and nanostructured cobalt oxide spinel nanoparticles does not make sense. Despite the goal of this experiment being just to point to the existence of the surface-related photoactivity of the cobalt oxide spinel nanoparticles, the observed sorption activity is likely a far better indicator of the enhanced specific surface properties of the nanostructured cobalt oxide spinel.

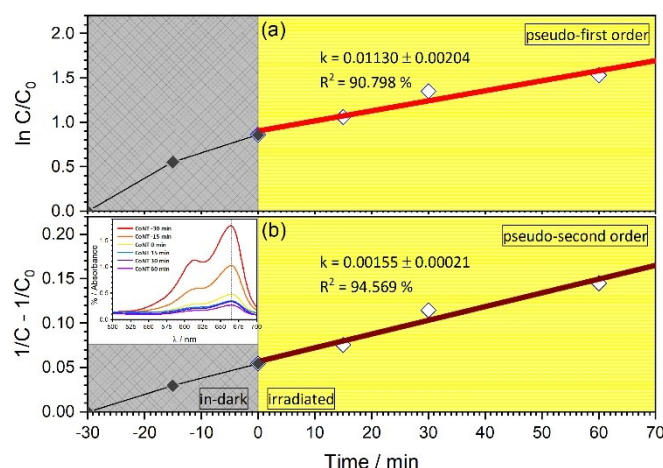


**Figure 9.** Indicative values for the sorption (−30–0 min, in dark) and photocatalytic degradation (0–60 min, irradiated) of the MB dye by the nanostructured cobalt oxide spinel photocatalyst for the case of: (a) pseudo-first-order fit of the photodegradation; (b) pseudo-second-order fit of the photodegradation. **Inset:** 500–700 nm segment of MB solution Vis spectra taken at various times.

In conclusion, previous characterisation results, including sorption/catalytic efficiency, nominate the developed nanostructured cobalt oxide materials for the photocatalytic application, especially for the degradation of harmful organic dyes. We wanted to test the gas-sensing performance as well but we encountered the boundaries of our system. Basically, the mass yield of our reactor was small, and thus, we were unable to collect sufficient mass to go through an optimisation process (trials and errors to match optimal content of the additives) for the preparation of films (of sufficient lateral size to accommodate heaters for sensing at temperatures normally above 300 °C and electrodes for electric performance testing) by tape casting (inherently a material-inefficient processing for small batches) [43]. Thus, some compromises in the context of the reactors for synthesis and testing are necessary to facilitate the desired scale-up of the material for gas sensing application, which nevertheless, are considered worth further development. It would be great if we could have performed sensing performance tests, but we consider that the demonstrated photocatalytically beneficial performance proved the viability of the prepared material. Reaching out to the synthesis and deposition route of  $\text{Co}_3\text{O}_4$  films in a single step would resolve the mentioned limitations and allow more reasonable scale-up efforts.

### 3. Materials and Methods

#### 3.1. Materials

The modified procedure was used for the synthesis [36]. Briefly, 10 mL of 0.1 M ammonia ( $\text{NH}_4\text{OH}$ , p.a. Kemika, Zagreb, Croatia) solution was slowly added to the 10 mL of 0.025 M nitrate solution prepared by dissolving cobalt nitrate hexahydrate ( $\text{Co}(\text{NO}_3)_2 \times 6\text{H}_2\text{O}$ , p.a. Kemika, Zagreb, Croatia) in demineralized water. After stirring for 30 min, the mixture was transferred in a 50 mL centrifuge tube and cobalt hydroxide precipitate was separated by centrifugation at 3500 rpm for 5 min. The precipitate was washed with deionized water and centrifuged. This procedure was repeated 6 times. Then, the precipitate was transferred in a 20 mL Teflon-lined autoclave. An amount of 0.3 g of sodium nitrate ( $\text{NaNO}_3$ , p.a. Kemika, Zagreb, Croatia), 8 mL of methanol ( $\text{CH}_3\text{OH}$ , p.a. Kemika, Zagreb, Croatia), and 8 mL of deionized water were then added. An autoclave was filled to 80% of the total volume and sealed, placed in a laboratory furnace, and heated at 235 °C for 36 h. After cooling, the washing procedure was repeated six more times as described previously. The derived materials were then dried at reduced pressure.

### 3.2. Methods

The powder X-ray diffraction (PXRD) was accomplished using the diffractometer XRD6000 (Shimadzu, Kyoto, Japan) with  $\text{CuK}\alpha$  radiation at an accelerating voltage of 40 kV and current of 30 mA. Data were collected between 15 and  $70^\circ 2\theta$ , in a step scan mode with steps of  $0.02^\circ$  and a counting time of 0.6 s. The average crystallite size was calculated from the broadening of the (311) diffraction peak using the Scherrer equation [44]:  $d = k\lambda/(\beta\cos\theta)$ , where  $d$  is the average crystallite diameter,  $k$  is the Scherrer constant (0.94),  $\lambda$  is the X-ray wavelength (0.15418 nm),  $\beta$  is the full-width at half-height of the (311) diffraction peak corrected for instrumental broadening, and  $\theta$  is the diffraction angle.

IR spectra were acquired using the Fourier Transform Infrared (FTIR) spectrometer Vertex 70 (Bruker, Billerica, MA, USA) in Attenuated Total Reflectance (ATR) mode. The samples were pressed on a diamond prism and the absorbance data were collected between 400 and  $4000\text{ cm}^{-1}$  with a spectral resolution of  $1\text{ cm}^{-1}$  and average of 64 scans.

The morphology was investigated with a Vega EasyProbe3 (Tescan, Brno, Czech Republic) Scanning Electron Microscope (SEM) operating at 30 kV. Samples for SEM characterization were fixed on a sample holder using double-sided carbon conductive tape, and then gold-coated using a SC 7620 sputter coater (Quorum, East Sussex, Laughton, UK).

The morphology was investigated with a JEM-ARM200F (Jeol, Tokyo, Japan) Transmission Electron Microscope (TEM). Powder samples for TEM characterization were ultrasonically dispersed and were placed on a copper mesh sample holder and subjected to analysis.

Simultaneous Thermogravimetric and Differential Thermal Analysis (TG-DTA) was accomplished using a STA 409C (Netzsch, Burlington, MA, USA). For the thermal analysis,  $\sim 50\text{ mg}$  of material was placed in Pt crucibles and heated at a rate of  $10\text{ }^\circ\text{C min}^{-1}$  to  $1300\text{ }^\circ\text{C}$  in a synthetic air flow of  $30\text{ cm}^3\text{ min}^{-1}$ , and  $\alpha$ -alumina was used as a reference.

The surface area was determined by nitrogen gas adsorption–desorption isotherms obtained at 77 K on ASAP-2000 equipment (Micromeritics Corporation, Norcross, GA, USA) using the Brunauer–Emmet–Teller model (BET). The samples were previously degassed at  $200\text{ }^\circ\text{C}$  under a dynamic vacuum of  $1.3\cdot 10^{-2}\text{ Pa}$ . Pore size distributions were calculated from desorption isotherms by the Barrett–Joyner–Halenda (BJH) model.

The photocatalytic activity was assessed using the methylene blue (MB) degradation test. For the photodegradation kinetics investigation,  $50\text{ mL}$  of  $25\text{ mgL}^{-1}$  of MB solution was poured in a borosilicate cylindrical glass vessel with a  $50\text{ mm}$  diameter and  $120\text{ mm}$  height. A quartz glass tube was placed in the vessel. An amount of  $50\text{ mg}$  of  $\text{Co}_3\text{O}_4$  was added to solution; thus, the photocatalyst concentration was  $1\text{ g L}^{-1}$ . A Pen Ray lamp (Analytik Jena GMBH, Upland, CA, USA), with a radiation wavelength of  $365\text{ nm}$  and emission intensity of  $2\text{ mW cm}^{-2}$ , was placed inside the quartz tube. The solution was first stirred for 30 min to establish adsorption equilibrium. After 30 min, the lamp was switched on and the photodegradation experiment was carried out at  $25\text{ }^\circ\text{C}$ . In order to determine the methylene blue concentration, aliquots of  $4\text{ mL}$  were withdrawn from the suspension at appropriate time intervals using a filter. The concentrations were determined using a UV–VIS spectrophotometer Cary 1E (Varian Inc., Palo Alto, CA, USA). For monitoring the concentration of MB, and hence its degradation, the absorption peak height at a wavelength of  $664\text{ nm}$  (where the maximum was) was used. The methylene blue concentration was computed using the previously established calibration curve.

## 4. Conclusions

A facile and affordable course of synthesis for the preparation of nanostructured cobalt oxide powders was shown in this study.

Diffraction analysis indicated the crystallisation of structurally monophasic  $\text{Co}_3\text{O}_4$  nanoparticles with a spinel structure. Infrared spectroscopy showed traces of organic phase in an otherwise chemically homogeneous material.

Scanning electron microscopy showed that the fine nanoparticle matter formed agglomerates. Transmission electron microscopy revealed that the agglomerates of the fine

nanoparticulated material actually consisted of 1D-shaped cobalt oxide spinel rods embedded in a fine nanoparticulated matrix. Nitrogen adsorption–desorption isotherms gave a sample-specific surface area of  $44.7 \text{ m}^2 \text{ g}^{-1}$  and enabled discussion of the orientation of the nanostructured material domains, exposure of nanostructured rods, and derivative geometry parameters. Thermal analysis showed that the nanostructured  $\text{Co}_3\text{O}_4$  material was stable up to  $800 \text{ }^\circ\text{C}$  where decomposition to  $\text{CoO}$  was observed.

On behalf of basic sorption/degradation tests, it was shown that the prepared nanostructured  $\text{Co}_3\text{O}_4$  materials had a chemical and (micro)structural background suitable for considering application as photocatalysts for the removal of the wastewater micropollutants, but also for continuation of the development of a single-step preparing route that would particularly favour gas-sensing application.

**Author Contributions:** Conceptualization, V.M. and S.K.; methodology, V.M., S.K., M.P. and I.P.; software, V.M., M.P. and I.P.; validation, V.M. and I.P.; formal analysis, V.M., M.P. and I.P.; investigation, V.M. and S.K.; resources, V.M. and S.K.; data curation, V.M. and I.P.; writing—original draft preparation, V.M. and S.K.; writing—review and editing, V.M.; visualization, V.M.; supervision, V.M.; project administration, V.M. and S.K.; funding acquisition, V.M. and S.K. All authors have read and agreed to the published version of the manuscript.

**Funding:** This work has been funded by the projects PZS-2019-02-1555 PV-WALL in the Research Cooperability Program of the Croatian Science Foundation funded by the European Union from the European Social Fund under the Operational Programme Efficient Human Resources 2014-2020 (TEM characterisation), UIP-2019-04-2367 SLIPPERY SLOPE (synthesis of material with reduced dimensionality), IP-2018-01-2963 HOUDINI (solvothermal synthesis), of the Croatian Science Foundation, and project KK.01.2.1.02.0316 by the European Regional Development Fund under the call Increasing the development of new products and services arising from research and development activities—phase II (photocatalytic test).

**Data Availability Statement:** The data behind this research are available upon reasonable request to corresponding author.

**Acknowledgments:** The sustenance of the University of Zagreb is gratefully acknowledged.

**Conflicts of Interest:** The authors declare no conflict of interest.

## References

1. Wagner, T.; Haffer, S.; Weinberger, C.; Klaus, D.; Tiemann, M. Mesoporous materials as gas sensors. *Chem. Soc. Rev.* **2013**, *42*, 4036–4053. [[CrossRef](#)]
2. Wang, C.X.; Yin, L.W.; Zhang, L.Y.; Xiang, D.; Gao, R. Metal oxide gas sensors: Sensitivity and influencing factors. *Sensors* **2010**, *10*, 2088–2106. [[CrossRef](#)]
3. Gu, C.D.; Zheng, H.; Wang, X.L.; Tu, J.P. Superior ethanol-sensing behavior based on  $\text{SnO}_2$  mesocrystals incorporating orthorhombic and tetragonal phases. *RSC Adv.* **2015**, *5*, 9143–9153. [[CrossRef](#)]
4. San, X.G.; Wang, G.S.; Liang, B.; Ma, J.; Meng, D.; Shen, Y.B. Flower-like  $\text{NiO}$  hierarchical microspheres self-assembled with nanosheets: Surfactant-free solvothermal synthesis and their gas sensing properties. *J. Alloys Compd.* **2015**, *636*, 357–362. [[CrossRef](#)]
5. Liu, X.C.; Hu, M.; Wang, Y.F.; Liu, J.F.; Qin, Y.X. High sensitivity  $\text{NO}_2$  sensor based on  $\text{CuO}/\text{p-porous silicon}$  heterojunction at room temperature. *J. Alloys Compd.* **2016**, *685*, 364–369. [[CrossRef](#)]
6. Yoon, J.W.; Kim, H.J.; Jeong, H.M.; Lee, J.H. Gas sensing characteristics of p-type  $\text{Cr}_2\text{O}_3$  and  $\text{Co}_3\text{O}_4$  nanofibers depending on inter-particle connectivity. *Sens. Actuator B Chem.* **2014**, *202*, 263–271. [[CrossRef](#)]
7. Kim, H.J.; Lee, J.H. Highly sensitive and selective gas sensors using p-type oxide semiconductors: Overview. *Sens. Actuator B Chem.* **2014**, *192*, 607–627. [[CrossRef](#)]
8. Ge, X.; Gu, C.D.; Wang, X.L.; Tu, J.P. Correlation between microstructure and electrochemical behavior of the mesoporous  $\text{Co}_3\text{O}_4$  sheet and its ionothermal synthesized hydrotalcite-like  $\text{a-Co(OH)}_2$  precursor. *J. Phys. Chem. C* **2014**, *118*, 911–923. [[CrossRef](#)]
9. Liang, Y.Y.; Li, Y.G.; Wang, H.L.; Zhou, J.G.; Wang, J.; Reigier, T.; Dai, H.J.  $\text{Co}_3\text{O}_4$  nanocrystals on graphene as a synergistic catalyst for oxygen reduction reaction. *Nat. Mater.* **2011**, *10*, 780–786. [[CrossRef](#)] [[PubMed](#)]
10. Xu, J.M.; Zhang, J.; Wang, B.B.; Liu, F. Shape-regulated synthesis of cobalt oxide and its gas-sensing property. *J. Alloys Compd.* **2015**, *619*, 361–367. [[CrossRef](#)]
11. Cheng, J.P.; Chen, X.; Wu, J.S.; Liu, F.; Zhang, X.B.; Dravid, V.P. Porous cobalt oxides with tunable hierarchical morphologies for supercapacitor electrodes. *CrystEngComm* **2012**, *14*, 6702–6709. [[CrossRef](#)]

12. Qiu, H.J.; Mu, Y.P.; Zhang, H.J.; Wang, Y. Designed synthesis of cobalt-oxide based nanomaterials for superior electrochemical energy storage devices. *Nano Res.* **2015**, *8*, 321–339. [[CrossRef](#)]
13. Vetter, S.; Haffer, S.; Wagner, T.; Tiemann, M. Nanostructured  $\text{Co}_3\text{O}_4$  as a CO gas sensor: Temperature-dependent behavior. *Sens. Actuator B Chem.* **2015**, *206*, 133–138. [[CrossRef](#)]
14. Farhadi, S.; Pourzare, K.; Sadeghinejad, S. Simple preparation of ferromagnetic  $\text{Co}_3\text{O}_4$  nanoparticles by thermal dissociation of the  $[\text{Co}(\text{NH}_3)_6](\text{NO}_3)_2$  complex at low temperature. *J. Nanostruct. Chem.* **2013**, *3*, 16. [[CrossRef](#)]
15. Akamatsu, T.; Itoh, T.; Izu, N.; Shin, W. NO and  $\text{NO}_2$  sensing properties of  $\text{WO}_3$  and  $\text{Co}_3\text{O}_4$  based gas sensor. *Sensors* **2013**, *13*, 12467–12481. [[CrossRef](#)]
16. Shaalan, M.N.; Rashad, M.; Moharram, A.H.; Abdel-Rahim, M.A. Promising methane gas sensor synthesized by microwave-assisted  $\text{Co}_3\text{O}_4$  nanoparticles. *Mat. Sci. Semicond. Proc.* **2016**, *46*, 1–5. [[CrossRef](#)]
17. Wang, X.; Tian, W.; Zhai, T.Y.; Zhi, C.Y.; Bando, Y.; Golberg, D. Cobalt(II,III) oxide hollow structures fabrication, properties and applications. *J. Mater. Chem.* **2012**, *22*, 23310–23326. [[CrossRef](#)]
18. Ma, L.Y.; Niu, B.; Xu, H.Y.; Cao, B.Q.; Wang, J.Q. Microwave hydrothermal synthesis of nanoporous cobalt oxides and their gas sensing properties. *Mater. Res. Bull.* **2011**, *46*, 1097–1101. [[CrossRef](#)]
19. Yoon, J.W.; Choi, J.K.; Lee, J.H. Design of a highly sensitive and selective  $\text{C}_2\text{H}_5\text{OH}$  sensor using p-type  $\text{Co}_3\text{O}_4$  nanofibers. *Sens. Actuator B Chem.* **2012**, *161*, 570–577. [[CrossRef](#)]
20. Nguye, H.; El-Safty, S.A. Meso- and macroporous  $\text{Co}_3\text{O}_4$  nanorods for effective VOC gas sensor. *J. Phys. Chem. C* **2011**, *115*, 8466–8474. [[CrossRef](#)]
21. Choi, K.I.; Kim, H.R.; Kim, K.M.; Liu, D.; Cao, G.; Lee, J.H.  $\text{C}_2\text{H}_5\text{OH}$  sensing characteristics of various  $\text{Co}_3\text{O}_4$  nanostructures prepared by solvothermal reaction. *Sens. Actuator B Chem.* **2010**, *146*, 183–189. [[CrossRef](#)]
22. Zhuo, L.; Ge, J.; Cao, L.; Wang, B. Solvothermal Synthesis of  $\text{CoO}$ ,  $\text{Co}_3\text{O}_4$ ,  $\text{Ni}(\text{OH})_2$  and  $\text{Mg}(\text{OH})_2$ . *Cryst. Growth Des.* **2009**, *9*, 1–6. [[CrossRef](#)]
23. Sun, L.; Li, H.; Ren, L.; Hu, C. Synthesis of  $\text{Co}_3\text{O}_4$  nanostructures using a solvothermal approach. *Solid State Sci.* **2009**, *11*, 108–112. [[CrossRef](#)]
24. Lou, X.; Han, J.; Chu, W.; Wang, X.; Cheng, Q. Synthesis and photocatalytic property of  $\text{Co}_3\text{O}_4$  nanorods. *Mater. Sci. Eng. B* **2007**, *137*, 268–271. [[CrossRef](#)]
25. Kohan, M.G.; Solomon, G.; You, S.; Yusupov, K.; Concina, I.; Vomiero, A. Vertically aligned  $\text{Co}_3\text{O}_4$  nanorods as platform for inverted all-oxide heterojunctions. *Nano Select.* **2021**, *2*, 967–978. [[CrossRef](#)]
26. Soni, V.; Xia, C.; Cheng, C.K.; Nguyen, V.H.; Nguyen, D.L.T.; Bajpai, A.; Kim, S.Y.; Van Le, Q.; Khan, A.A.P.; Singh, P.; et al. Advances and recent trends in cobalt-based cocatalysts for solar-to-fuel conversion. *Appl. Mater. Today* **2021**, *24*, 101074. [[CrossRef](#)]
27. Sonu; Dutta, V.; Sharma, S.; Raizada, P.; Hosseini-Bandegharai, A.; Gupta, V.K.; Singh, P. Review on augmentation in photocatalytic activity of  $\text{CoFe}_2\text{O}_4$  via heterojunction formation for photocatalysis of organic pollutants in water. *J. Saudi Chem. Soc.* **2019**, *23*, 1119–1136. [[CrossRef](#)]
28. Chandel, N.; Sharma, K.; Sudhaik, A.; Raizada, P.; Hosseini-Bandegharai, A.; Thakur, V.K.; Singh, P. Magnetically separable  $\text{ZnO}/\text{ZnFe}_2\text{O}_4$  and  $\text{ZnO}/\text{CoFe}_2\text{O}_4$  photocatalysts supported onto nitrogen doped graphene for photocatalytic degradation of toxic dyes. *Arab. J. Chem.* **2020**, *2*, 4324–4340. [[CrossRef](#)]
29. Yan, W.; Xu, Y.; Hao, S.; He, Z.; Wang, L.; Wei, Q.; Xu, Q.; Tang, H. Promoting charge separation in hollow-structured  $\text{C}/\text{MoS}_2@/\text{ZnIn}_2\text{S}_4/\text{Co}_3\text{O}_4$  photocatalysts via double heterojunctions for enhanced photocatalytic hydrogen evolution. *Inorg. Chem.* **2022**, *61*, 4275–4734. [[CrossRef](#)]
30. Chen, X.; Cheng, J.P.; Shou, Q.L.; Liu, F.; Zhang, X.B. Effect of calcinations temperature on the porous structure of cobalt oxide micro-flowers. *Cryst. Eng. Comm.* **2012**, *14*, 1271–1276. [[CrossRef](#)]
31. Cheng, J.P.; Liu, L.; Zhang, J.; Liu, F.; Zhang, X.B. Influences of anion exchange and phase transformation on the supercapacitive properties of  $\alpha\text{-Co}(\text{OH})_2$ . *J. Electroanal. Chem.* **2014**, *722*, 23–31. [[CrossRef](#)]
32. Yuan, Y.F.; Xia, X.H.; Wu, J.B.; Huang, X.H.; Pei, Y.B.; Yang, J.L.; Guo, S.Y. Hierarchically porous  $\text{Co}_3\text{O}_4$  film with mesoporous walls prepared via liquid crystalline template for supercapacitor application. *Electrochem. Commun.* **2011**, *13*, 1123–1126. [[CrossRef](#)]
33. Patil, D.; Patil, P.; Subramanian, V.; Joy, P.A.; Potdar, H.S. Highly sensitive and fast responding CO sensor based on  $\text{Co}_3\text{O}_4$  nanorods. *Talanta* **2010**, *81*, 37–43. [[CrossRef](#)] [[PubMed](#)]
34. Wen, Z.; Zhu, L.P.; Mei, W.M.; Hu, L.; Li, Y.G.; Sun, L.W.; Cai, H.; Ye, Z.Z. Rhombus-shaped  $\text{Co}_3\text{O}_4$  nanorod arrays for high-performance gas sensor. *Sens. Actuator B Chem.* **2013**, *186*, 172–179. [[CrossRef](#)]
35. Warang, T.; Patel, N.; Santini, A.; Bazzanella, N.; Kale, A.; Miotello, A. Pulsed laser deposition of  $\text{Co}_3\text{O}_4$  nanoparticles assembled coating: Role of substrate temperature to tailor disordered to crystalline phase and related photocatalytic activity in degradation of methylene blue. *Appl. Catal. A Gen.* **2012**, *423*, 21–27. [[CrossRef](#)]
36. Xia, F.; Ou, E.; Wang, L.; Wang, J. Photocatalytic degradation of dyes over cobalt doped mesoporous SBA-15 under sunlight. *Dye. Pigment.* **2008**, *76*, 76–81. [[CrossRef](#)]
37. Makhlof, M.T.; Abu-Zied, B.M.; Mansoure, T.H. Direct Fabrication of Cobalt Oxide Nanoparticles Employing Sucrose as a Combustion Fuel. *J. Nanopart. Res.* **2013**, *2013*, 384350. [[CrossRef](#)]
38. Kaczmarczyk, J.; Zasada, F.; Janas, J.; Indyka, P.; Piskorz, W.; Kotarba, A.; Sojka, Z. Thermodynamic Stability, Redox Properties, and Reactivity of  $\text{Mn}_3\text{O}_4$ ,  $\text{Fe}_3\text{O}_4$ , and  $\text{Co}_3\text{O}_4$  Model Catalysts for  $\text{N}_2\text{O}$  Decomposition: Resolving the Origins of Steady Turnover. *ACS Catal.* **2016**, *6*, 1235–1246. [[CrossRef](#)]

39. Wang, L.; Maxisch, T.; Ceder, G. A First-Principles Approach to Studying the Thermal Stability of Oxide Cathode Materials. *Chem. Mater.* **2007**, *19*, 543–552. [[CrossRef](#)]
40. Sing, K.S.W.; Everett, D.H.; Haul, R.A.W.; Moscou, L.; Pierotti, R.A.; Rouquerol, J.; Siemieniewska, T. Reporting Physisorption Data for Gas/Solid Systems with Special Reference to the Determination of Surface Area and Porosity. *Pure Appl. Chem.* **1985**, *57*, 603–619. [[CrossRef](#)]
41. Kumarage, G.W.C.; Comini, E. Low-Dimensional Nanostructures Based on Cobalt Oxide (Co<sub>3</sub>O<sub>4</sub>) in Chemical-Gas Sensing. *Chemosensors* **2021**, *9*, 197. [[CrossRef](#)]
42. Verma, M.; Mitan, M.; Kim, H.; Vaya, D. Efficient photocatalytic degradation of Malachite green dye using facilely synthesized cobalt oxide nanomaterials using citric acid and oleic acid. *J. Phys. Chem. Solids* **2021**, *155*, 110125. [[CrossRef](#)]
43. Suwanchawalit, C. High Photocatalytic Performance of Magnetic CoFe<sub>2</sub>O<sub>4</sub>-Graphene Nanocomposite for Organic Dye Removal. *Aust. J. Basic Appl. Sci.* **2015**, *9*, 159–165.
44. Klug, H.P.; Alexander, L.E. *X-Ray Diffraction Procedures*, 2nd ed.; John Wiley & Sons Inc.: New York, NY, USA, 1974; pp. 687–703.